Chinese Journal of
POLYMER SCIENCE

RESEARCH ARTICLE

https://doi.org/10.1007/s10118-026-3657-y
Chinese J. Polym. Sci.

Amphiphilic Hyaluronic Acids Enhance Sanshool's Efficacy against Skin Photodamage *via* Stability Improvement and Cell Cycle Regulation

Yi Yang[a,b], Jun-Mei Song[c], Tian-You Wang[c], Shu-Wei Wu[a,b], Yu-Hang Zhou[c], Zhi-Peng Gu[c*], Ling-Hong Guo[a,b*], and Xian Jiang[a,b*]

[a] *Department of Dermatology, West China Hospital, Sichuan University, Chengdu 610041, China*
[b] *Laboratory of Dermatology, Clinical Institute of Inflammation and Immunology, Frontiers Science Center for Disease-related Molecular Network, West China Hospital, Chengdu 610041, China*
[c] *College of Polymer Science and Engineering, State Key Laboratory of Advanced Polymer Materials, Sichuan University, Chengdu 610065, China*

Electronic Supplementary Information

Abstract Sanshool is a promising skin photoprotective agent with strong UV absorption and great antioxidative activity. However, it faces challenges including poor stability, skin penetration-associated systemic toxicity, and efficacy loss upon chemical modification. To address these issues, amphiphilic hyaluronic acids (HHA) were synthesized and self-assembled to integrate with sanshool *via* hydrophobic interactions, significantly boosting its photostability by 24% and enhancing its antioxidative activity. In HaCaT cells, HHA-sanshool nanoparticles (NPs) reduced UVB-induced reactive oxygen species, decreased cell apoptosis, and lowered G2/M phase arrest from 42% to approximately 31% (close to the normal level), while also inhibiting excessive autophagy. Moreover, in a mouse model, HHA-sanshool NPs alleviated UVB-induced skin damage, reducing skin thickening by up to 50% and mitigating erythema, protected collagen/elastic fibers, and suppressed proinflammatory factor, with no dermal penetration *in vivo*. This strategy provides a simple, efficient and safe platform for natural active molecular clinical translation in skin photoprotection.

Keywords Hyaluronic acid; Sanshool; Nanoplatform; Stability improvement; Cell cycle regulation

Citation: Yang, Y.; Song, J. M.; Wang, T. Y.; Wu, S. W.; Zhou, Y. H.; Gu, Z. P.; Guo, L. H.; Jiang, X. Amphiphilic hyaluronic acids enhance sanshool's efficacy against skin photodamage *via* stability improvement and cell cycle regulation. *Chinese J. Polym. Sci.* https://doi.org/10.1007/s10118-026-3657-y

INTRODUCTION

Long-term exposure to ultraviolet (UV) radiation can cause severe photodamage to the skin, which destroys the first line of defense for the human body against external environmental insults.[1,2] UV radiation triggers the release of reactive oxygen species (ROS),[3,4] secretion of pro-inflammatory factors, and DNA damage, which leads to collagen degradation, disruption of the barrier function, and cell cycle disorders, ultimately resulting in rough skin, pigmentation, and even cancerization.[5–9] In particular, disruption of the cell cycle caused by light loss severely impedes the normal renewal and repair of the skin, making it difficult to restore the healthy state of the skin. Although physical blockers (such as titanium dioxide and zinc oxide) to diffuse UV and chemical absorbers (such as benzophenone and avobenzone) to absorb UV have been utilized for current clinical photoprotection, the therapeutic effect on photodamage has been severely limited by the phototoxicity of physical agents, as well as the transdermal and migratory properties of chemical agents.[10–14] Moreover, traditional strategies focus only on UV shielding but lack intervention in skin cell physiology after photodamage, such as the inflammatory cascade response and cell cycle regulation,[15–17] making it difficult to meet the needs of multi-targeted synergistic treatment. In addition, the widespread adoption of novel bio-based sun-protective materials has been limited by their high costs, complex fabrication processes, and suboptimal effectiveness.[18–20] Thus, the development of new functional materials that are highly efficient in photoprotection and in evaluating precise pathological mechanisms has become a key challenge in the field of anti-photodamage.

Plants have evolved strategies to secrete specific metabolites to protect against light damage, providing a valuable natural source for the development of new photoprotective materials.[21–23] Sanshool, an alkylamide derived from *Zanthoxylum xanthoxylum*, exhibits outstanding antioxidative,

* Corresponding authors, E-mail: guzhipeng2019@scu.edu.cn (Z.P.G.)
E-mail: linhom.guo@foxmail.com (L.H.G.)
E-mail: jiangxian@scu.edu.cn (X.J.)
Received February 12, 2026; Accepted March 11, 2026; Published online April 16, 2026

anti-inflammatory, and photoprotective activities, owing to its unique conjugated diene structure. Notably, sanshool has been shown to directly scavenge free radicals, modulate key cellular signaling pathways involved in inflammation and apoptosis, and protect skin cells from UVB-induced damage, positioning it as a promising candidate among natural small molecules for combating skin photoaging.[24] Previous studies have shown that sanshool can significantly alleviate UVB-induced light damage by inhibiting ROS generation and fibroblast apoptosis.[25] However, its small molecular nature makes it prone to percutaneous penetration and potential systemic toxicity. Additionally, its poor chemical stability and strict storage conditions severely limit its practical applications.[26–29] Some strategies for nature-inspired sanshool-based nanomaterials have been explored, and improvements in sanshool stability have been demonstrated.[25,30] However, specific chemical modifications (such as borate esterification) are required to serve materials construction, which may alter the natural active structure of the plant-derived bioactive molecules and affect their physiological activity.[31] Therefore, achieving stable, safe, and efficient targeted delivery[32] of pristine plant efficacy molecules, including sanshool, while preserving their structural integrity and biological activity remains a core challenge in the field.

Hyaluronic acid (HA) is a natural biological macromolecule that is widely distributed in the extracellular matrix of connective tissues and plays a key role in cell signaling, wound healing, joint lubrication, and skin hydration.[33,34] Due to its excellent biocompatibility and non-immunogenicity, HA is widely recognized as a safe biomaterial with high affinity for human tissues, making it an ideal candidate for biomedical and cosmetic applications. More than half of the total HA in the human body is localized in the skin, where it not only contributes to tissue hydration and biological adhesion, but also actively participates in maintaining skin homeostasis, regulating cell proliferation, and facilitating tissue repair through interactions with cellular receptors.[35,36] However, its pronounced hydrophilicity hinders direct interaction with highly hydrophobic molecules, including sanshool, thereby necessitating ingenious modification or functionalization strategies to expand its application scope in delivery systems. To this end, chemical modifications of HA, particularly covalent conjugation of hydrophobic moieties, have been extensively explored to engineer amphiphilic derivatives. These tailored polymers can self-assemble into core-shell nanostructures in aqueous environments, thereby transforming native HA into a versatile delivery vehicle capable of encapsulating hydrophobic actives, enhancing their stability, and enabling slow release.[37–39] Our work builds upon this established principle by employing hydrophobic modifications to create a stable and efficacious system for sanshool delivery.

In this study, amphiphilic hyaluronic acid (HHA) was constructed through hydrophobic chain modification, enabling subsequent molecular self-assembly in aqueous environments. Driven by hydrophobic interactions, amphiphilic polymers spontaneously organize into core-shell nanostructures, with hydrophobic segments forming an inner core for efficient sanshool encapsulation and hydrophilic HA chains extending outward to form a stabilizing shell. This self-assembly process not only markedly improves sanshool stability, but also preserves the inherent bioactivity of the carbohydrate polymer, allowing the resulting HHA-based nanoparticles to maintain skin affinity and biocompatibility (Fig. 1).[40,41] This design leverages hydrophobic-grafted HA to encapsulate sanshool efficiently, while the hydrophilic HA shell ensures colloidal stability, promotes skin adhesion, and regulates local retention. The present study systematically evaluated the physicochemical properties, stability, and *in vitro* photoprotective efficacy of NPs, and further explored their mechanisms in mitigating UV-induced damage through modulation of inflammatory, oxidative, and homeostatic pathways. By integrating the biocompatibility and tunability of HA with a non-covalent loading strategy, this study provides a rational and translatable platform for the topical delivery of labile natural compounds, thereby offering a novel therapeutic avenue for anti-photoaging interventions.

EXPERIMENTAL

Materials

Hyaluronic acid ($M_w \approx 150$ kDa, purity≥98%, research-grade) was purchased from Shanghai Maclin Biochemical Technology Co., Ltd. Ethylene glycol dicarboxylic acid (EDC, 98%) was purchased from Hela Aladdin Biochemical Technology Co., Ltd. *N*-Hydroxysuccinimide (NHS, 98%) was purchased from Hela Aladdin Biochemical Technology Co., Ltd. Octadecylamine (95%), oleylamine (98%), and 3,3-diphenylpropylamine (98%) were all purchased from Shanghai Titan Technology Co., Ltd. Dimethylformamide (DMF, 99.9%) was purchased from Beijing Inokai Technology Co., Ltd. Ethanol (99.9%) was purchased from Shanghai Titan Technology Co., Ltd. and sanshool (95% from HPLC) was obtained from the laboratory-purified *Zanthoxylum xanthoxylum* extract.

Cell Counting Kit-8 (Beyotime, C0037), Annexin V-EGFP/PI Double Staining Apoptosis Detection Assay (Kai Ji Biology, KGA1101-10), Autophagy Indicator (mRFP-GFP-LC3) (Hanbio Hanheng Biology, HB-AP2100001), Reactive Oxygen Species Assay Kit (Yi Sheng Biotechnology Co., Ltd., 50101ES01), Hoechst 33258 solution (LABELAD, 23491-45-4), JC-1 Mitochondrial Membrane Potential Detection Kit (UElandy, J6004S), and Cell Cycle Detection Kit (Kai Ji Biology, KGA9101-100) were used.

Material Preparation

Synthesis of HHA

Amphiphilic HA derivatives were synthesized *via* EDC/NHS-mediated amidation with the aim of systematically modulating the hydrophobicity and self-assembly behavior by grafting hydrophobic fragments with different degrees of conjugation and chemical structures. Briefly, 100 mg of HA was dissolved in 10 mL of deionized water, followed by the addition of 100 mg of EDC and 60 mg of NHS to activate the carboxyl groups under stirring for 6 h at room temperature. Then, an equimolar amount (0.263 mmol) of hydrophobic amine (specifically, 71.1 mg of octadecylamine, 76.1 mg of oleamide, or 55.8 mg of 3,3-diphenylpropylamine) dissolved in 5 mL of DMF was added dropwise. The reaction proceeded at 60 °C for 5 h, and subsequently at room temperature for 24 h. The crude product was purified by centrifugation (at 5000 r/min for 3 min) to remove

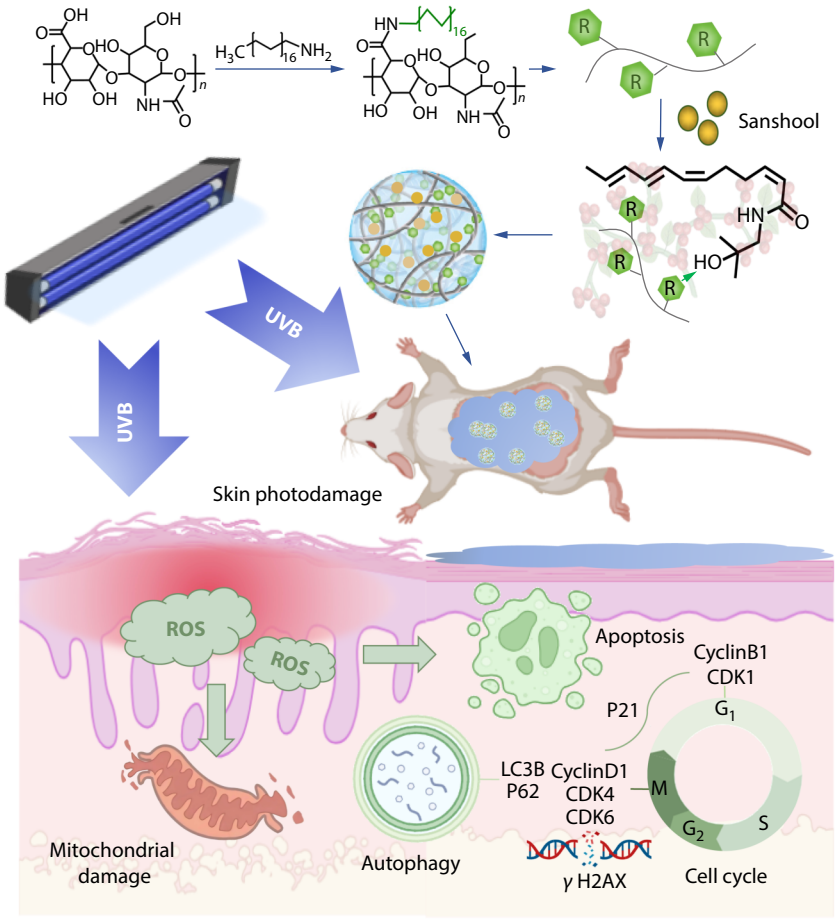

Fig. 1 Diagram and illustration of HA-assisted sanshool based nanoplatform with improved stabilities and functions against skin photodamage.

insoluble aggregates. Then, The supernatant was transferred to a dialysis membrane (with a molecular cut-off of 3.5 kDa) and was dialyzed successively with a series of gradient concentrations of ethanol/water mixtures (70%, 50%, and 30% ethanol, volume ratio, 24 h each time) to gradually remove the toxic organic solvent DMF. Subsequently, it was dialyzed with deionized water (with the water changed every 6–8 h) to ensure the complete removal of residual organic solvents and water-soluble by-products. After filtration through a 0.45 μm membrane, the solution was lyophilized to obtain the corresponding polymers, denoted as HHA*i* (where *i*=1–3; 1 is grafted with octadecylamine, 2 is grafted with oleamide, 3 is grafted with 3,3-diphenylpropylamine), respectively.

Preparation of HHA-sanshool NPs

HHA-sanshool NPs were prepared using dialysis. For each polymer (HHA1-3), 10 mg of polymer and 50 mg of sanshool (1:5 mass ratio) were dissolved in 5 mL of DMSO under light protection. After stirring for 1 h, the solution was dialyzed (MWCO 3.5 kDa) against deionized water in the dark for 24 h. Finally, NPs formulations were obtained, denoted as SO1, SO2, and SO3 (SO1-3 correspond to HHA1-3 of the assembled sanshool). Blank NPs were prepared in a similar manner without sanshool.

Light stability test

Sanshool, SO1, SO2, and SO3 solutions (50 μg/mL) were prepared using deionized water. A UV-visible spectrophotometer was used to record the initial absorbance (A_0) at 271 nm wavelength. After the samples were treated with simulated sunlight (2 W, 10 cm vertical irradiation from the sample) for different periods of time, measure the absorbance (A_t) and calculate the retention rate ($A_t/A_0 \times 100\%$).

Cell culture and UVB treatment

Human immortalized keratinocyte cells (HaCaT) were cultured in MEM (Minimum Essential Medium) medium containing 10% fetal bovine serum (FBS). All cell experiments were divided into six groups: normal control (NC), UVB damage, sanshool, SO1, SO2, and SO3 groups. Except for the NC group, the cells in the other groups were pre-treated in drug-containing medium (with the same concentration of materials containing sanshool and SO1-3 in each group) for 24 h, and then exposed to 80 mJ/cm^2 UVB (homerry SH4B, 311 nm). The optimal photoprotective concentration of HHA-sanshool NPs was determined to be 10 μg/mL (soluble in MEM), which was used in subsequent experiments.

Apoptosis test

Cell apoptosis was detected using the Annexin V-EGFP/PI Apoptosis Detection Kit following the manufacturer's protocol. After treatment, the harvested HaCaT cells were resuspended in binding buffer and stained with 5 μL of Annexin V-EGFP and 5 μL of PI for 15 min at room temperature in the dark. The samples were immediately analyzed by flow cytometry. Annexin V-EGFP fluorescence was detected in the FITC channel (Ex = 488 nm, Em = 530 nm), and PI in the PE channel (Ex = 488 nm, Em =

575 nm). Data from 1×10^4 events per sample were collected and analyzed using the FlowJo software.

Observation of Autophagy

Autophagy was monitored using an mRFP-GFP-LC3 Adenovirus Indicator (HB-AP2100001; Hanbio). HaCaT cells were infected with the adenovirus at an MOI of 20 for 24 h. Where applicable, the cells were treated with 100 nmol/L bafilomycin A1 for 4 h prior to imaging. The cells were observed using a confocal microscope (Leica TCS SP8) with a 63× oil immersion objective. mRFP was excited at 561 nm and GFP was excited at 488 nm. Images were analyzed using ImageJ software, and autophagic flux was quantified by counting the number of mRFP+GFP+ (autophagosomes) and mRFP+GFP − (autolysosomes) puncta per cell.

Cell cycle analysis

Cell cycle distribution was analyzed using a Cell Cycle Detection Kit (Kai Ji Biology, KGA9101-100). After treatment, cells were fixed in 70% ethanol at 4 °C for 24 h. Fixed cells were then incubated with 0.5 mg/mL propidium iodide (PI) staining solution containing 0.1 mg/mL RNase A for 30 min at 37 °C in the dark. The DNA content was analyzed by flow cytometry using the PE channel (Ex = 488 nm, Em = 617 nm), with a minimum of 1×10^4 events collected per sample. Data analysis was performed using the FlowJo software to determine the percentage of cells in the G0/G1, S, and G2/M phases.

Animal experiment

All animal experimental procedures were approved by the Ethics Committee of West China Hospital of Sichuan University (20220223116). All mice were 6-8-week-old SPF-grade female BALB/c mice, with a body weight of approximately 18–22 g. The environmental temperature was maintained at 18–29 °C, and the relative humidity was controlled at 40%–70%. Mice were randomly divided into 6 groups: NC, UVB, Sanshool, SO1, SO2, and SO3. Except for the NC group, the other groups received UVB irradiation for 5 consecutive days (300 seconds per day, cumulative 1.5 J/cm^2), and 0.3 mL of the corresponding drug solution (2 mg/mL solution of sanshool and SO1-3 in water) was applied before each light exposure.

Skin Appearance Assessment and Histological Examination

Daily photographs of the back skin of the mice were obtained. The degree of light damage was scored (0–2 points) according to the standard, and the thickness of the skinfold was measured. Skin tissues were collected, fixed with 4% paraformaldehyde, embedded in paraffin, sectioned, and stained with Hematoxylin-Eosin staining (H&E). Morphological changes in the tissues were observed under an optical microscope.

RESULTS AND DISCUSSION

Preparation and Characterization of HA-sanshool NPs

First, we modified the classic carbohydrate polymer HA using various hydrophobic structures (including octadecylamine, oleoylamine, and 3,3-diphenylpropylamine) through an amideation reaction to obtain HHA*i* (*i*=1–3) with customized hydrophobic features (Fig. 2a). The structures of these modified carbohydrate polymers were characterized by Fourier transform infrared spectroscopy (FTIR) and nuclear magnetic resonance (NMR) spectroscopy. The success of the grafting reaction was confirmed by the shifts in the hydroxyl peak and the characteristic peaks of the carbon chain and benzene ring (Fig. 2b). Further ^{1}H-NMR analysis determined the grafting ratios of these three hydrophobic basic units to be 55.17%, 48.33%, and 33.64%, respectively, calculated based on the integral area ratio of the characteristic proton signals of the grafted hydrophobic chains to those of the HA backbone (Fig. 2c). Subsequently, sanshool (Fig. S1 in the electronic supplementary information, ESI) was induced, and HHA-sanshool NPs were prepared through hydrophobic-hydrophilic interactions between sanshool and the modified HHA, and they were named as SO1-3 NPs. The morphology of the prepared NPs was spherical and uniformly dispersed by scanning electron microscopy (SEM) and dynamic light scattering (DLS) (Fig. 2d). Subsequently, the average particle size and zeta potential of SO1-3 NPs in pure water, PBS, and MEM were measured (Fig. 2e, Figs. S2 and S3 in ESI). As shown in the results, the NPs exhibited uniform dispersion in all the three solvent systems. The corresponding zeta potential values were negative across all conditions, with absolute values exceeding 35 mV, indicating that strong electrostatic repulsion between

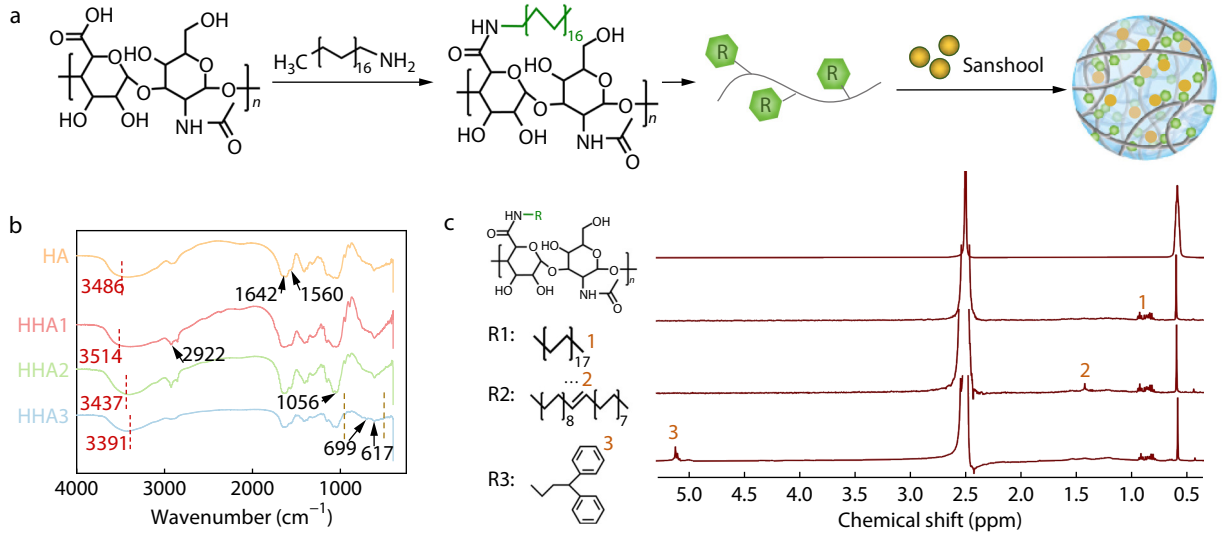

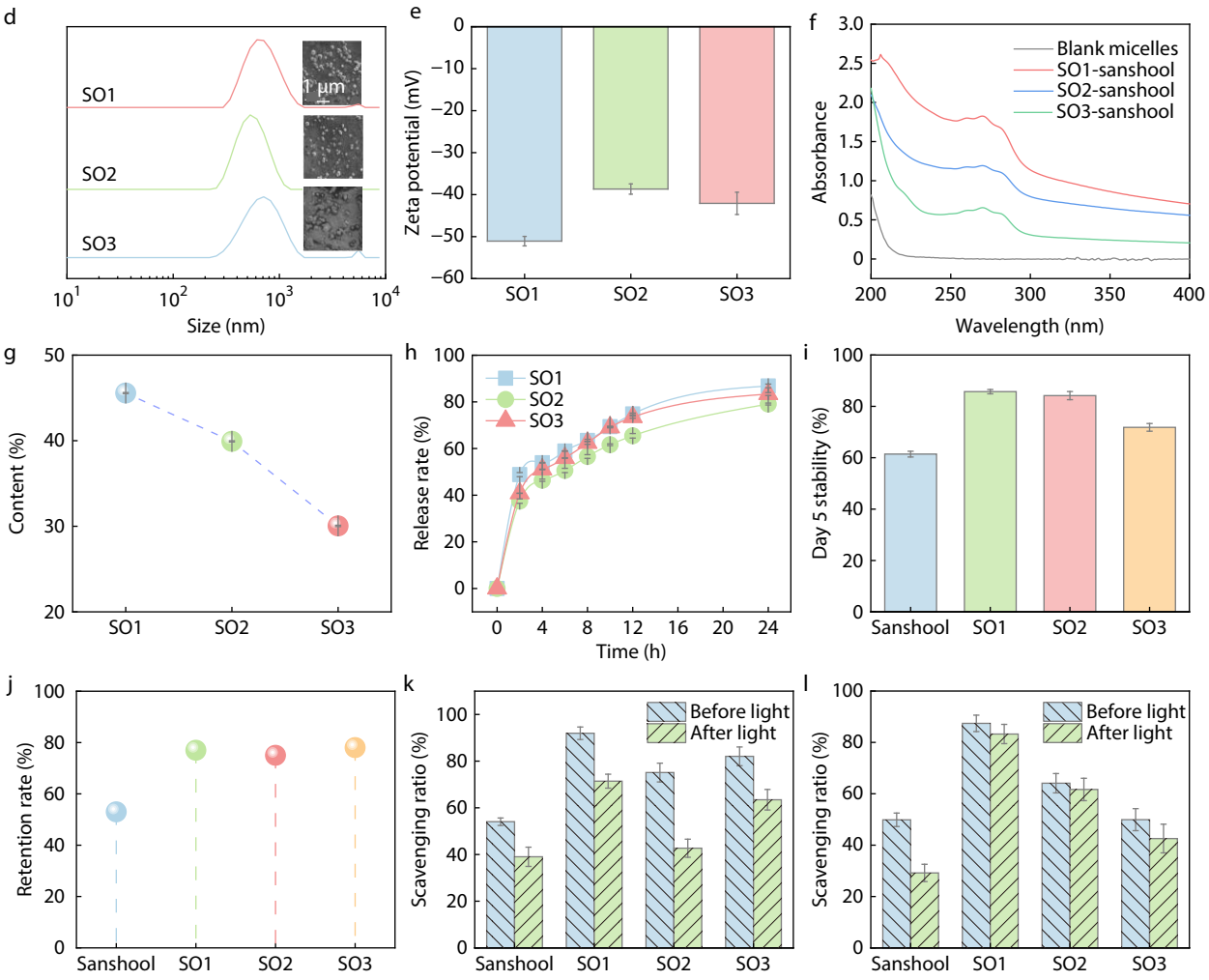

Fig. 2 Preparation and Characterization of HHA-Sanshool NPs. (a) Schematic diagram of HHA-assisted sanshool based nanoplatform synthesis; (b) The FTIR spectra and (c) NMR spectra of HHA*i* (*i*=1–3) modified by octadecylamine, oleamide and 3,3-diphenylpropylamine, as well as pure HA; (d) The particle size distribution and SEM images of the prepared SO1-3 NPs; (e) The Zeta plot of SO1-3 NPs in pure water; (f) The UV spectra of the 50 μg/mL SO1-3 NPs solution and the blank NPs without sanshool added; (g) The content of sanshool in 1 mg/mL of SO1-3 NPs; (h) The release rate of sanshool from SO1-3 NPs after 24 h of release in PBS (pH=7.4); (i) The statistics of sanshool content after storage of 1 mg/mL of sanshool and SO1-3 NPs at room temperature for 5 days to obtain the stability at room temperature; (j) The statistics of sanshool content in the materials after exposure to simulated sunlight for 2 h at 1 mg/mL of sanshool and SO1-3 NPs, to obtain the light stability; The scavenging rates of (k) ABTS and (l) DPPH by sanshool and SO1-3 NPs at 120 min before and after 2 h of light exposure.

particles effectively prevented aggregation and ensured excellent colloidal stability of the formulations. The ultraviolet-visible spectra of sanshool and SO1-3 were recorded, and the results showed that sanshool and all NPs had strong absorption in the UVB region (Fig. 2f and Fig. S4 in ESI), and the maximum absorbance occurred at 271 nm. The sanshool content was detected by the absorbance value of the ultraviolet characteristic peak, and it was found that the SO1-2 NPs possessed a higher sanshool loading efficiency because of the longer hydrophobic chain structure (Fig. 2g and Fig. S5 in ESI). Interestingly, all SO1-3 NPs exhibited a sustained release characteristic of sanshool for up to 24 h (Fig. 2h and Fig. S6 in ESI), which was attributed to their abundant dynamic non-covalent interactions. More importantly, all the prepared NPs showed significantly improved storage stability compared to bare sanshool (Fig. 2i and Fig. S7 in ESI). Based on these highly convincing characteristics, further studies were conducted on the properties of SO1-3. Notably, compared to sanshool, the absorbance retention of SO1-3 increased after 2 h of ultraviolet irradiation (Fig. 2, Figs. S8 and S9 in ESI), indicating an improvement in its protection against ultraviolet radiation. Additionally, the prepared NPs effectively retained the inherent antioxidative activity of sanshool and exhibited significant scavenging ability against typical free radicals (Figs. 2k–2l and Fig. S10 in ESI). Owing to the instability of the unique structure under ultraviolet radiation, the antioxidative performance of sanshool sharply declined after ultraviolet irradiation. Interestingly, the designed strategy significantly improved the antioxidant stability of the sanshool. In particular, SO1 maintained 71.42% and 83.27% free radical scavenging activity after ultraviolet irradiation, whereas sanshool only retained 39.03% and 29.19%.

Photoprotective Effect of HHA-sanshool NPs

To evaluate the photoprotective performance of HHA-sanshool

NPs, HaCaT skin cells were chosen as the model cell line. (Fig. 3a). As a carrier, HA exhibits excellent cell compatibility primarily owing to its inherent presence in the extracellular matrix. It can form a hydrated biomimetic environment and can be specifically recognized by cell surface receptors[42] thereby actively regulating cell adhesion, proliferation, and migration.[43] Before that, the biocompatibility of the prepared HHA-sanshool NPs (SO1-3) was tested using the Cell Counting Kit-8 (CCK-8) assay. Notably, within a certain concentration range (5–15 μg/mL), the survival rate of HaCaT cells under the action of each group of materials was greater than 70%, which might be attributed to the structural encapsulation of sanshool (Fig. 3b). To further assess the photoprotective efficacy of the prepared NPs, HaCaT cells were pre-treated with SO1-3 NPs and naked sanshool at a unified concentration of 10 μg/mL, followed by exposure to high-intensity UVB radiation (Fig. 3c). The CCK-8 assay results confirmed that all SO1-3 groups outperformed free sanshool in protecting cells against UVB-induced damage. Previous studies have also demonstrated that UVB radiation activates multiple deleterious signaling cascades in HaCaT cells, particularly autophagy induction and keratinocyte apoptosis.[44] As evidenced by flow cytometry, UVB exposure significantly elevated the early apoptotic, late apoptotic, and total apoptotic levels in HaCaT cells (Figs. 3d and 3e). In contrast, the pro-apoptotic effect of UVB was markedly attenuated in cells pre-treated with SO1-3 or naked sanshool. Notably, SO1 displayed the strongest anti-apoptotic activity among the three groups, which was closely associated with its advantages of stability improvement and higher loading contents.

In addition to investigating the regulatory effects on apoptosis, we further explored the autophagic behavior of HaCaT cells. Autophagy is a conserved cellular process that involves the encapsulation of damaged organelles and macromolecules into vesicles (autophagosomes) for subsequent

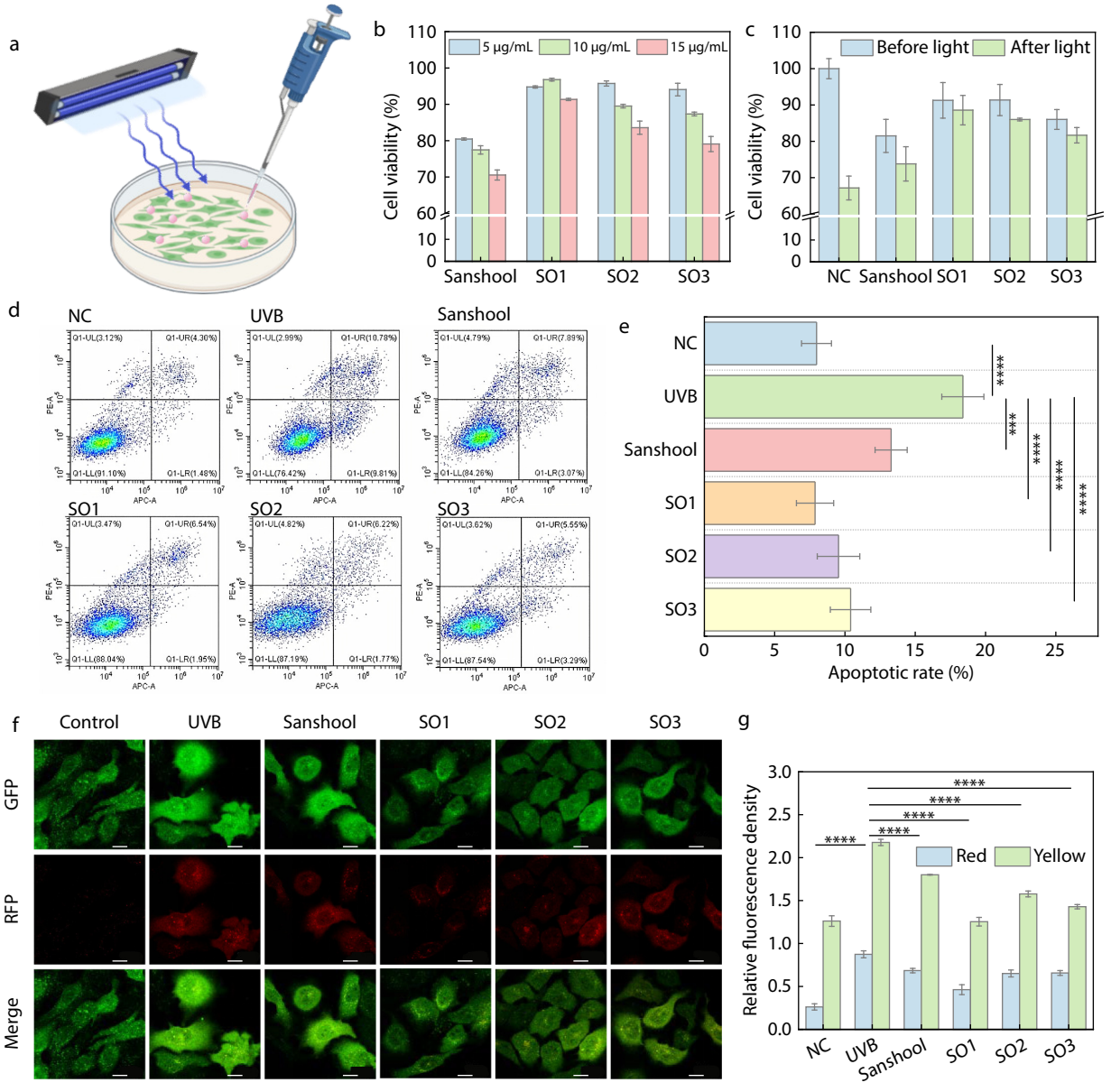

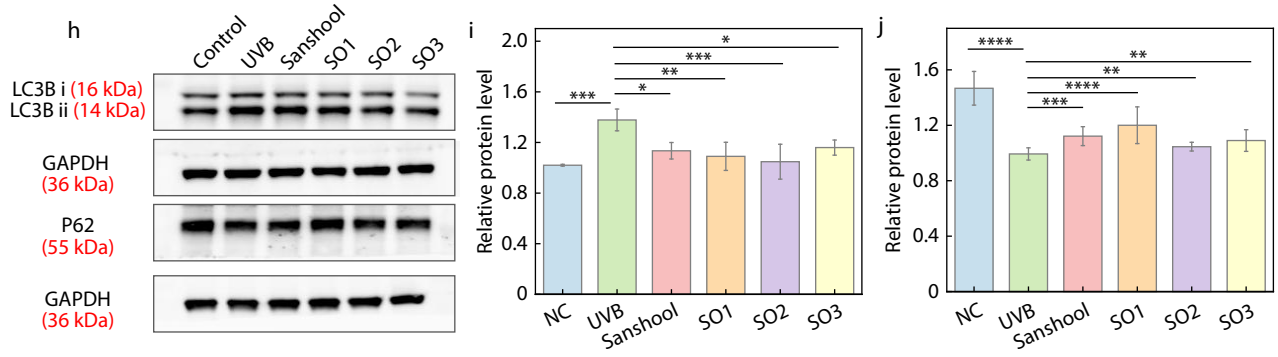

Fig. 3 The photoprotective effect of HA-sanshool NPs. (a) Diagram of cell experiment, after treating HaCaT cells with materials and UVB irradiation, subsequent tests were conducted; (b) Detection of cell survival rate using CCK-8 reagent after treating HaCaT cells with different concentrations of sanshool and SO1-3 NPs; (c) Cell survival rate before and after UVB irradiation with 10 μg/mL sanshool and SO1-3 NPs; (d, e) Cell apoptosis graphs and statistics of apoptotic cell content after 10 μg/mL sanshool and SO1-3 NPs treatment after UVB irradiation; (f, g) Study on the effect of autophagic flux on materials-treated HaCaT cells after UVB irradiation (adenovirus Ad-GFP-mRFP-LC3) (The scale bars in Fig. 3f are 10 μm); (h) Detection of LC3BI, LC3BII and P62 protein expression in HaCaT cells treated with materials and UVB using Western blotting; (i) Statistical analysis of LC3II/I ratio after treatment with materials and UVB (n=3); (j) Statistical analysis of P62 expression level after treatment with materials and UVB (n=3). A two-independent-sample t-test was used for comparison between groups, and $^*p < 0.05$ was considered statistically significant. NS: not significant, $^*p < 0.05$, $^{**}p < 0.01$, $^{***}p < 0.001$.

degradation, thereby recycling small molecules and energy to maintain cellular homeostasis.[45] LC3 is co-labeled with green fluorescent protein (GFP) and red fluorescent protein (mRFP). When autophagosomes fuse with lysosomes, because lysosomes are acidic and GFP is sensitive to acidity, green fluorescence is quenched, and only red fluorescence representing mRFP can be detected. Therefore, the yellow spots (the merge of green and red fluorescence) represent autophagosomes (early autophagy), and the red spots represent autophagic lysosomes (late autophagy). The strength of the autophagic flow is indicated by the number of yellow and red spots. Confocal laser scanning microscopy (CLSM) images and quantitative statistics (Figs. 3f and 3g) revealed that UVB irradiation significantly increased the density and fluorescence intensity of autophagosome vesicles in HaCaT cells, indicating that UVB exposure induced a notable upregulation of autophagic flux in cells. In contrast, pretreatment with sanshool and SO1-3 NPs, particularly in the SO1 group, markedly abrogated the UVB-induced increase in autophagosome density and fluorescence intensity. This result demonstrated that sanshool-based NPs can effectively mitigate the excessive elevation of autophagic flux triggered by UVB-induced photodamage. The initiation and progression of autophagy is tightly regulated by a series of autophagy-related (ATG) gene products. A well-recognized hallmark of enhanced autophagic activity is an increased ratio of microtubule-associated protein 1 light chain 3 II to I (LC3 II:I), accompanied by downregulated expression level of P62. Consistent with the CLSM imaging results, western blot analysis showed that UVB irradiation significantly elevated the LC3 II/I ratio in HaCaT cells. Pretreatment with sanshool and HHA-sanshool NPs (SO1-3) notably reduced this ratio. Similarly, compared with the UVB-irradiated group (UV group), HaCaT cells pre-treated with sanshool and HHA-sanshool NPs (SO1-3) showed significant upregulation of P62 expression (Figs. 3h–3j, Figs. S11 and S12 in ESI). These findings clearly confirm that HHA loading does not interfere with the regulatory effect of sanshool on the autophagic pathway; instead, its slow release ability (Fig. 2h) may facilitate this regulatory effect by maintaining a continuous and effective concentration of sanshool in the cellular microenvironment. Collectively, the above results demonstrate that sanshool can effectively suppress the excessive elevation of autophagic flux induced by UVB photodamage, whereas HHA encapsulation can enhance the potent protective effect.

In vivo Photoprotective Assessment

Before initiating *in vivo* photoprotection studies, it is essential to evaluate skin adhesive performance to ensure the formation of a continuous yet removable protective barrier against UVB and to verify skin permeability to minimize the risk of systemic toxicity. (Fig. 4a) To evaluate these properties, SO1-3 NPs were labeled with fluorescein isothiocyanate (FITC) and uniformly applied to the dorsal skin of mice. The fluorescence signals were monitored at different time points using an *in vivo* imaging system (IVIS). The results showed that After rinsing with water, the fluorescence intensity of FITC-labeled sanshool and SO1-3 NPs remained unchanged, indicating good water resistance (Fig. 4b). When wiped with alcohol, the fluorescence signals of the SO1-3 NPs were nearly eliminated, demonstrating favorable erasability. However, the free sanshool group exhibited persistently strong fluorescence, even after alcohol wiping. These results confirmed that HHA-sanshool NPs outperformed free sanshool in terms of water resistance and controllable removability, which are key characteristics for practical skin protection applications. Adhesiveness is an important indicator for evaluating skin material. Over time, the fluorescence signals of sanshool and SO3 on the surface of the nude mice skin were significantly weakened (Fig. 4c), while the fluorescence signals of SO1 and SO2 remained unchanged, proving that SO1-2 has good adhesion and stability. Permeation toxicity is an important safety concern in cosmetics. It is evaluated by observing frozen sections to assess the skin penetration properties. As shown in Fig. 4(d), the fluorescence signal of free sanshool was distributed on the skin surface and was still detectable in the superficial dermis, indicating potential penetration and associated toxicity risks.

Further quantitative analysis also demonstrated that the construction of nanomaterials significantly reduced skin permeability (Fig. S13 in ESI). This phenomenon was likely attributed to the significant skin permeability of free sanshool, which allowed it to penetrate the stratum corneum and accumulate in the deeper skin layers. In striking contrast, FITC-labeled SO1-3 NPs exhibited fluorescence signals strictly limited to the skin surface. This localization was attributed to the high molecular weight of HHA, which effectively reduced skin penetration of sanshool and eliminated penetration-related toxicity risks.

Subsequently, a mouse model of UVB-induced skin photodamage was established to assess the *in vivo* protective efficacy of the HHA-sanshool NPs. Mice were shaved on the dorsal region and irradiated with UVB daily, and free sanshool or SO1-3 NPs were applied via quantitative coating 30 min before each irradiation. On the fifth day of light exposure, the skin of the unprotected mice became significantly thicker and showed obvious redness, scabs, and other damage (Fig. 4e). The free sanshool group exhibited a certain level of protective capability, and SO1-3 NPs showed superior protective effects that markedly alleviated dorsal skin damage, reduced the swollen area and scale count, and normalized the skin thickness. Specifically, the dorsal skin of SO1-treated mice had a thinner epidermal-dermal bilayer and a lower photodamage score than all other UVB-irradiated groups (Figs. 4f, 4g and Fig. S14 in ESI). Histopathological analysis of skin tissues was performed to comprehensively characterize the protective effects (Fig. 4h). After UVB-induced photodamage,

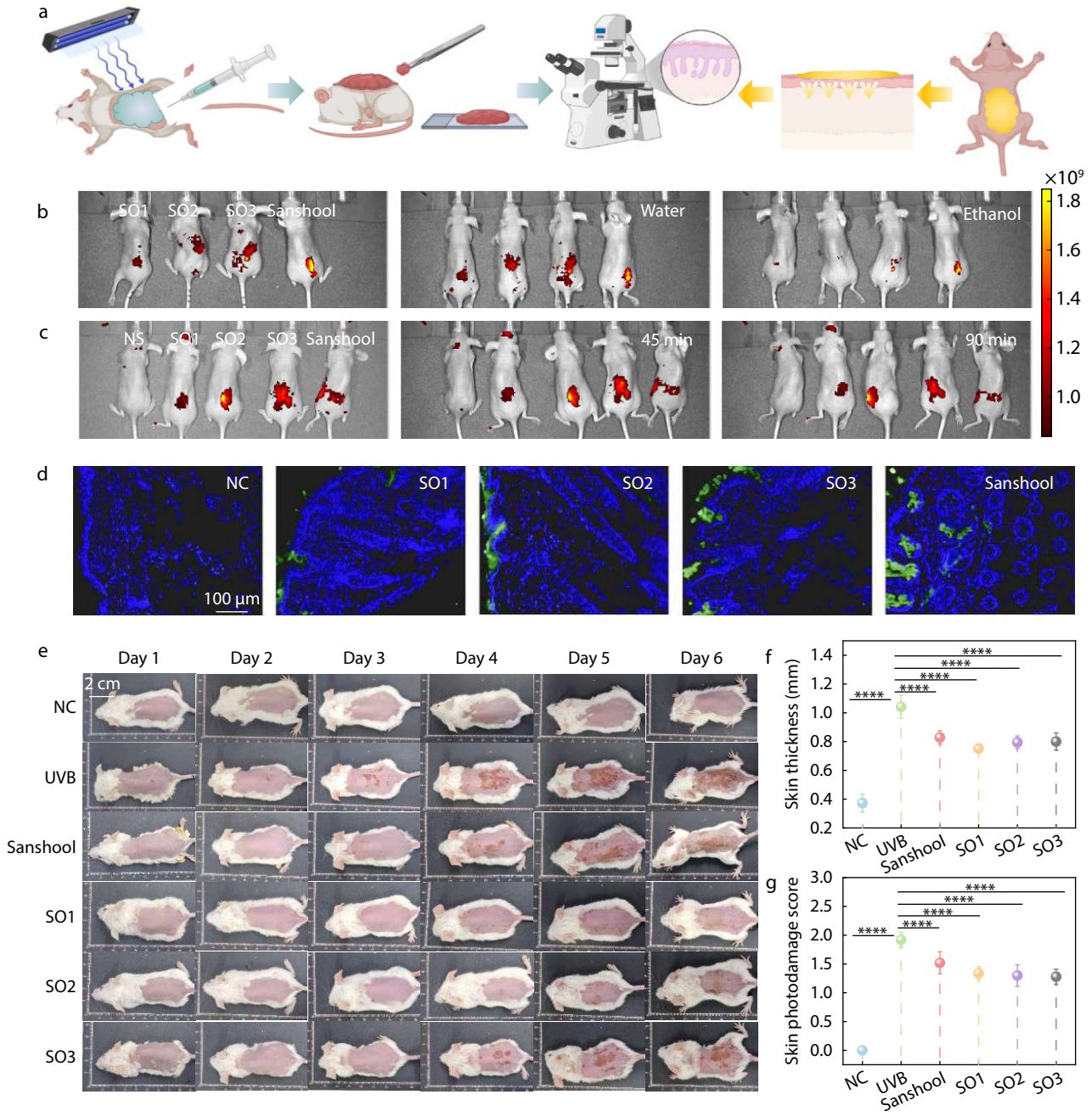

https://doi.org/10.1007/s10118-026-3657-y

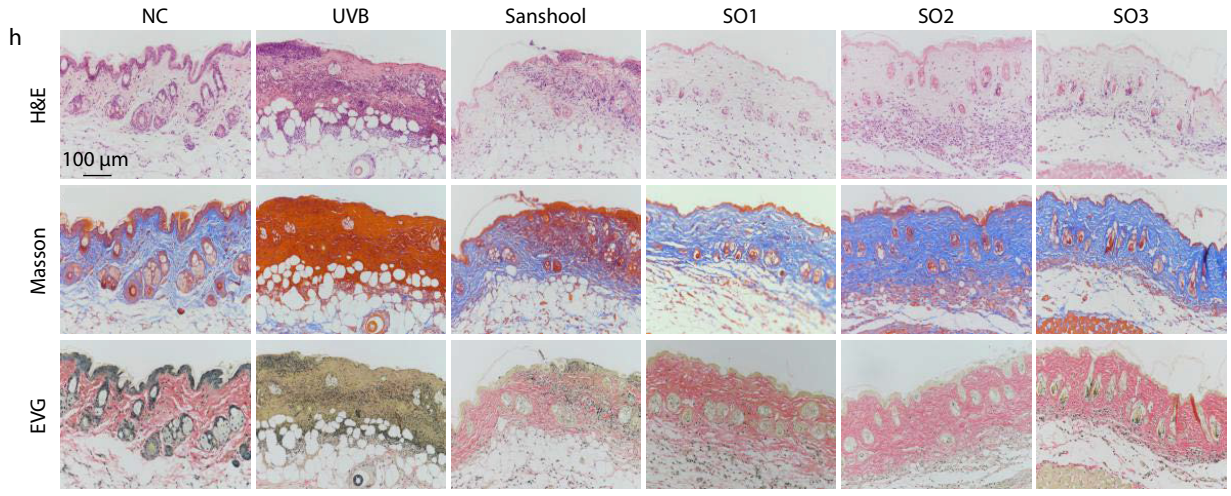

Fig. 4 *In vivo* photoprotective assessment. (a) Diagram of animal experiment: modeling of light-damaged mice and histological sections of skin tissue, live imaging to statistically analyze fluorescence intensity; (b) Live imaging to statistically observe the retention of sanshool and SO1-3 NPs on the back skin of mice after washing with water and wiping with alcohol; (c) Live imaging to statistically observe the adhesion of sanshool and SO1-3 NPs on the back skin of mice after 90 min; (d) Frozen section observation of the adhesion of sanshool and SO1-3 NPs on the skin of mice for 4 h, to evaluate the transdermal properties of the materials; (e) Back skin condition of mice after daily light exposure; (f) Detection of mouse back skin thickness on the 6^{th} day after material treatment and light exposure; (g) Back skin damage score of mice on the 6^{th} day after material treatment and light exposure; (h) H&E staining to observe the morphological characteristics of the skin tissue, Masson staining method to evaluate the morphology and expression of collagen fibers in the dermis of the mouse skin, EVG staining to observe the morphology of elastic fibers. NS: not significant, $*p < 0.05$, $**p < 0.01$, $***p < 0.001$.

hematoxylin-eosin (H&E) staining showed that the epidermal layer exhibited obvious irregular thickening, which is a typical pathological feature of UVB-induced epidermal hyperplasia. Masson's staining with specific markers for collagen fibers revealed that the collagen fiber structure in the dermis of the UVB group was severely damaged, showing obvious structural damage. Elastic fibers stained with Elastic Van Gieson (EVC) appeared disorganized and degenerated. In contrast, treatment with free sanshool and HHA-sanshool NPs collectively mitigated these photodamage-induced pathological changes, with the SO1 group exhibiting the most prominent protective effect. The epidermal layer skin of mice in the SO1 group was significantly thinner, the collagen fiber bundles in the dermis were arranged neatly and uniformly with loose inter-fiber gaps, and most of the elastic fiber structures had clear and normal morphologies. Of all formulations, SO1 NPs demonstrated the most pronounced protective efficacy, which can be attributed to their optimally engineered structure. The octadecylamine-modified HHA backbone achieves an ideal balance between hydrophilicity and lipophilicity. This molecular design resulted in a uniform distribution and superior stability. These rationally designed features collectively improve sanshool bioavailability and prolong its retention in the skin tissues, thereby maximizing its therapeutic potential against photodamage. These differences in histopathological results further indicated that the photodamage-protective effect of HHA-sanshool NPs was superior to that of free sanshool, which was attributed to the designed strategies in material engineering.

Photoprotective Mechanism

Given the significant *in vivo* photoprotective efficacy of HHA-sanshool NPs observed in a mouse skin photodamage model, we further investigated the underlying molecular mechanisms governing their protective effects. UVB irradiation is known to trigger the excessive generation of reactive oxygen species (ROS) while impairing intracellular ROS balance systems,[46] thereby initiating oxidative stress responses that directly induce cellular and tissue damage. To evaluate the intracellular free radical-scavenging capacity of HHA-sanshool NPs, 2,7-dichlorodihydrofluorescein diacetate (DCFH-DA), a specific fluorescent probe for ROS, was used to detect intracellular ROS levels. CLSM images (Fig. 5a) clearly demonstrated that UVB exposure drastically elevated the ROS fluorescence intensity in HaCaT cells, reflecting a marked increase in intracellular ROS accumulation. In contrast, pretreatment with SO1-3 NPs significantly attenuated the UVB-induced ROS overproduction. Quantitative validation using flow cytometry further confirmed this trend (Figs. 5b, 5c and Fig. S15 in ESI). Notably, the SO3 group maintained relatively high ROS levels, which was presumably attributed to its lower sanshool loading efficiency and more unstable hydrophobic-hydrophilic interactions, leading to insufficient release of active sanshool for ROS scavenging.

Further measurements of intracellular superoxide dismutase (SOD) levels were conducted to assess oxidative damage. The expression levels of SOD in all the SO1-3 NPs groups were higher than those in the sanshool treatment group (Fig. 5d), indicating that UV-induced cellular oxidative damage was significantly alleviated. Excessive ROS can also cause damage to the mitochondria, and the integrity of the mitochondrial membrane can be evaluated by JC-1 staining and CLSM. As shown in Figs. 5(e)–5(g), compared to the control group, unprotected cells showed a reduction in red fluorescence and an increase in green fluorescence after UVB irradiation, directly indicating mitochondrial dysfunction. In contrast, cells protected by SO1-3 could prevent mitochondrial membrane depolarization and effectively maintain mitochondrial function.

https://doi.org/10.1007/s10118-026-3657-y

In addition, changes in ROS can trigger the production of a series of pro-inflammatory factors, such as interleukin (IL)-6 and tumor necrosis factor (TNF)-*α*,[47] achieved by upregulating secondary mediators in macrophages and mesenchymal cells, thereby stimulating the synthesis of acute-phase proteins.[48] Immunohistochemical staining and immunofluorescence staining for interleukin-6 (IL-6) and tumor necrosis factor-*α* (TNF)-*α* provided clear histological evidence of skin inflammation induced by UVB radiation and also demonstrated the therapeutic effect of SO1-3 NPs (Fig. 5h). The tissue sec-

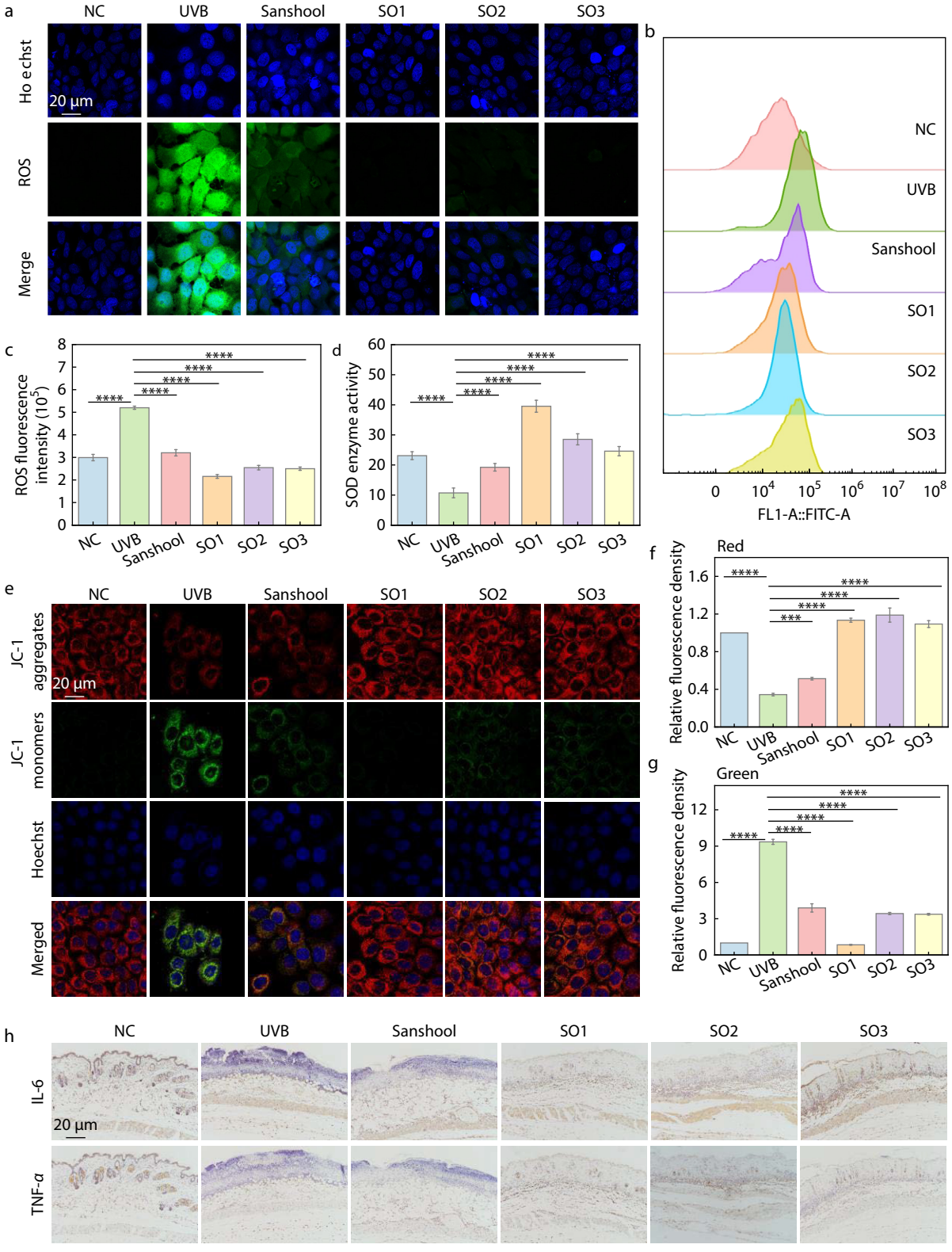

https://doi.org/10.1007/s10118-026-3657-y

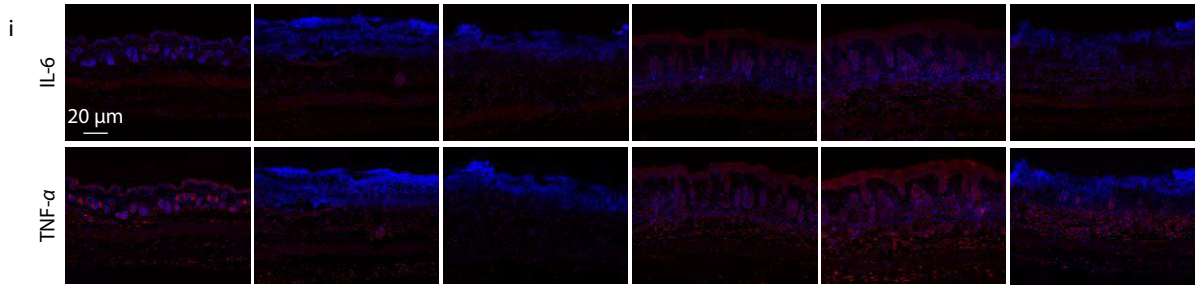

Fig. 5 Exploration of the photoprotective molecular mechanism. (a) Fluorescence confocal images of ROS levels obtained through DAPI, DCFH-DA, and combined staining methods, with Hoechst 33258 dye for cell nucleus localization; (b) Quantitative detection of ROS levels in the six groups of cells after illumination by flow cytometry; (c) Statistical analysis of ROS fluorescence intensity in each group after illumination; (d) Detection of SOD enzyme activity levels of the six groups of cells after illumination using the WST-8 method at the same protein concentration; (e) The effect of JC-1 reagent on protecting the mitochondrial membrane depolarization of HaCaT cells; (f, g) Statistical graphs of red and green fluorescence intensities after JC-1 reagent staining of the six groups of cells. The immunohistochemical staining of inflammatory factors TNF-*α* and IL-6 (h) and the immunofluorescence staining (i) were performed to observe the skin inflammatory response. *$p < 0.05$, **$p < 0.01$, ***$p < 0.001$.

tions from the UVB group showed a strong positive signal, mainly concentrated in the cytoplasm of epidermal keratinocytes, especially in the stratum spinosum and the granular layer. In contrast, sections from the SO1-3 NP treatment group showed significantly reduced intensity and range of staining. Immunofluorescence staining revealed a pronounced pro-inflammatory response following UVB exposure, characterized by intense and widespread cytoplasmic fluorescence signals for both IL-6 and (TNF)-*α* within the epidermal and dermal compartments (Fig. 5i). This indicated a significant upregulation of these key inflammatory cytokines. In contrast, tissues treated with SO1-3 NPs post-UVB irradiation exhibited markedly diminished fluorescence intensity, with signal distribution and strength closely resembling those observed in the non-irradiated normal control group. Notably, the attenuation effect was most robust in the SO1 subgroup, where the fluorescent signals for IL-6 and TNF-*α* were nearly completely suppressed, demonstrating its superior anti-inflammatory efficacy compared with the sanshool treatment group. These visual findings, consistent with parallel immunohistochemistry data, quantitatively confirm that SO1-3 NPs, particularly SO1, effectively restore UVB-disrupted inflammatory homeostasis to basal levels. This superior performance can be attributed to the rationally designed amphiphilic structure of the HA derivatives. The octadecylamine modification with optimal chain length facilitated the stable encapsulation of sanshool through hydrophobic interactions while maintaining an appropriate hydrophilicity-lipophilicity balance. The preserved bioactivity of sanshool within the NPs system coupled with the intrinsic biocompatibility of the HA backbone collectively contributed to the optimized therapeutic outcome, validating the effectiveness of this carbohydrate-based nanocarrier design for enhancing the anti-photoaging potential of natural compounds.

Cell Cycle Regulation

Building on our previous findings, UVB irradiation induces cell cycle disorder, which is a key pathological feature of skin photodamage. We further explored the molecular mechanisms by which HHA-sanshool NPs regulate the cell cycle of UVB-damaged HaCaT cells (Fig. 6a). Generally, normal HaCaT cells exhibit a characteristic cell cycle distribution in which the majority reside in the G1 phase, with a small subset progressing through the S phase (DNA synthesis) and G2/M phase (mitosis)).[49] As shown in Figs. 6(b) and 6(c), when cells were exposed to UVB radiation, they initiated cell cycle arrest as a protective response, pausing proliferation to gain time to repair DNA damage.[50] The replication in the S phase was slow, but the cells in the G1 phase entered normally, resulting in an increase in the number of S1 phase cells, while mitosis in the G2/M phase was inhibited, leading to an increase in the proportion of G2/M phase cells. As photodamage-protective materials, sanshool and SO1-3 NPs have the ability to scavenge free radicals and promote DNA repair. In cells treated with sanshool and SO1-3 NPs, ROS and DNA damage caused by UVB were significantly reduced, thereby reducing the number of cells in the G2/M phase. At the same time, a large number of G1 phase cells entered the S phase, resulting in an increase in the proportion. Compared with the UVB irradiation group, the proportion of HaCaT cells in the G2/M phase in the SO1-3 NPs group was significantly reduced. SO1-3 NPs effectively protected cells from photodamage by inhibiting UVB-induced apoptosis and cell cycle arrest. The key factors regulating the cell cycle include cyclin-dependent kinases (CDKs) and cyclins, which jointly promote cell transition at different stages of the cell cycle. CDK1 mainly participates in the transition from G2/M, whereas CyclinD usually binds to CDK4/6 to regulate the transition from G1/S (Fig. 6a). We quantitatively measured the expression of CDK1 and CyclinD by Western blotting (Figs. 6d–6f, Figs. S16–S17 in ESI), The results showed that the expression levels of CDK1 and CyclinD in HaCaT cells after UVB irradiation were significantly reduced, and their expression levels returned to normal after SO1-3 treatment.

The ROS produced by UVB can cause oxidative DNA damage, involving the rapid phosphorylation of histone H2AX at Ser139 to form *γ*-H2AX, a sensitive marker of DNA double-strand breaks.[51] Concurrently, cell cycle checkpoint protein p21 (CDKN1A), a key downstream target of the tumor suppressor p53, is transcriptionally upregulated. p21 functions as a potent cyclin-dependent kinase inhibitor (CKI), halting cell cycle progression at both G1/S and G2/M transitions to allow time for DNA repair.[52] Our Western blot analysis confirmed this mechanistic response to UVB irradiation, demonstrating a significant increase in the protein levels of both *γ*-H2AX and

p21 in HaCaT cells (Figs. 6g–6i, Figs. S18 and S19 in ESI). This elevation signifies the activation of the DNA damage checkpoint and initiation of protective cell cycle arrest. Importantly, treatment with the photoprotective agent SO1-3 NPs effectively mitigated this damage signal, as evidenced by the restoration of γ-H2AX and p21 protein levels to near-normal

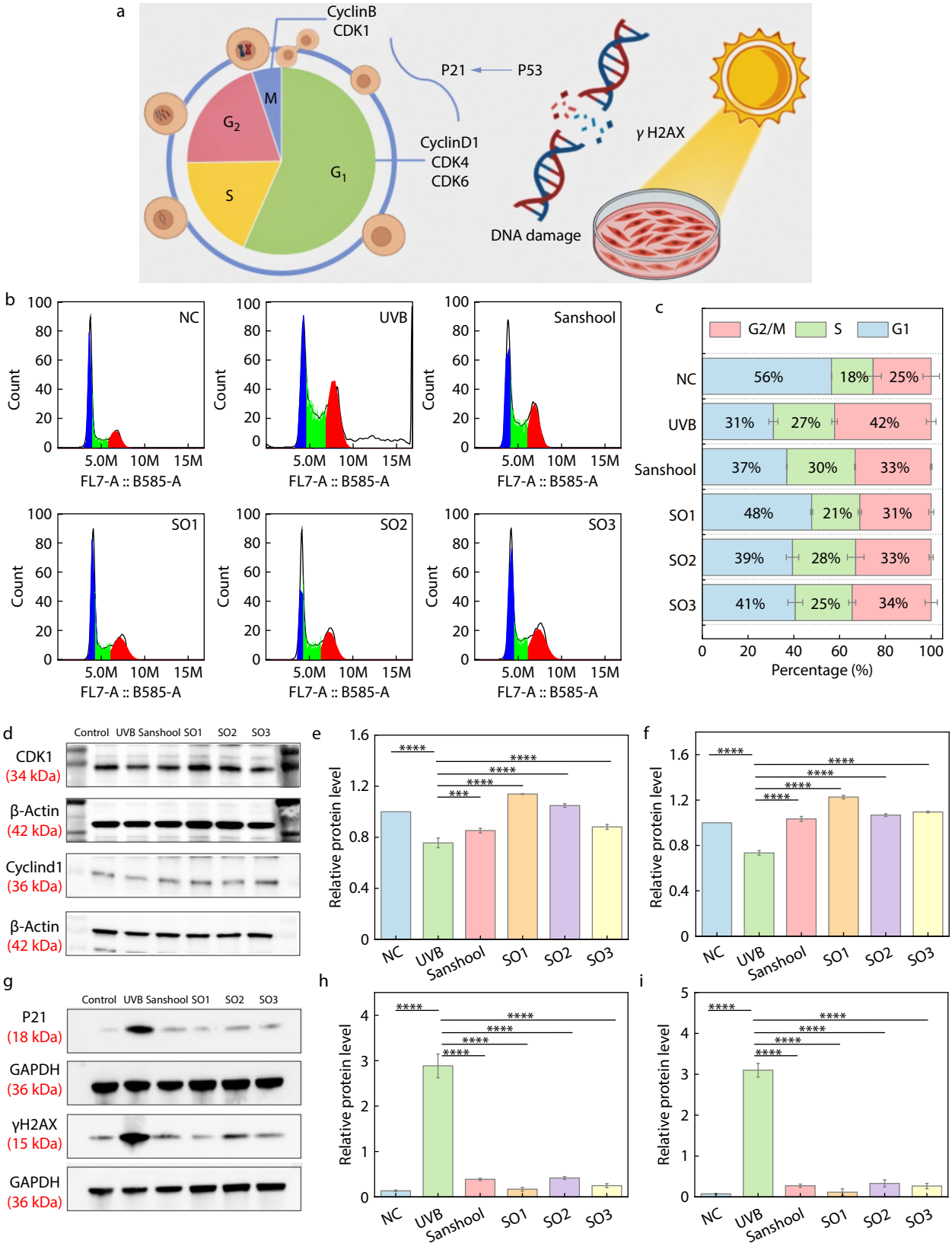

https://doi.org/10.1007/s10118-026-3657-y

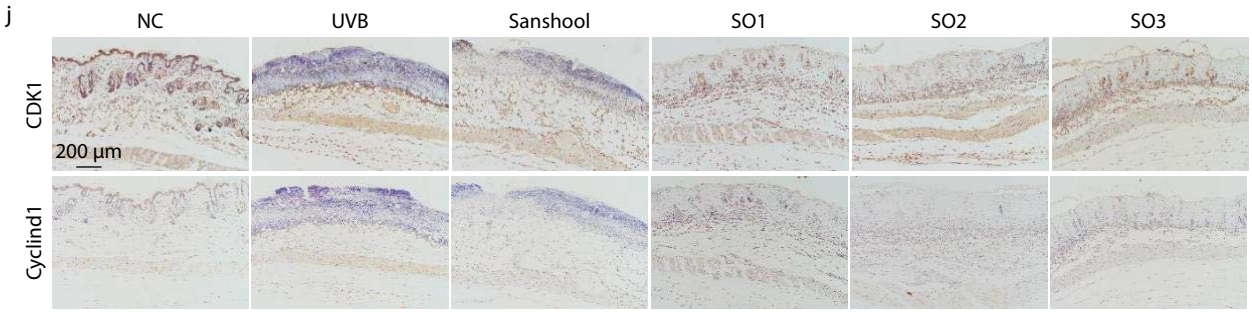

Fig. 6 Exploration of cell cycle regulation. (a) Diagram showing the effects of UVB irradiation on the cell cycle process and related proteins; (b) After UVB treatment, PI/RNase A staining was performed and the cell cycle distribution was detected by flow cytometry (M represented million); (c) Statistical graph showing the changes in the cycle distribution ratio of each group after light treatment; (d) Western Blot method was used to detect the expression of cyclin CDK1 and cyclind in HaCaT cells treated with the materials and UVB irradiation (n=3); (e, f) Statistical analysis of the expression levels of cyclind and CDK1 after material and UVB treatment (n=3); (g) Western Blot method was used to detect the expression of related proteins P21 and γH2AX in HaCaT cells treated with the materials after UVB irradiation. (h, i) Statistical analysis of the expression levels of P21 and γH2AX after treatment with the materials and UVB (n=3); (j) Staining of cyclind and CDK1 in skin sections for observing the distribution of cyclins. NS: not significant, *p < 0.05, **p < 0.01, ***p < 0.001.

baseline levels, consistent with the observed alleviation of cell cycle arrest. The CDK1 and CyclinD staining sections (Fig. 6j) showed that the levels of CDK1 and CyclinD in the tissue significantly decreased after UVB exposure, and the inhibitory effect of the SO1 group on cell cycle arrest was significantly better than that of the sanshool group. This enhanced protective effect originates from the rationally designed amphiphilic architecture of HA-based nanocarriers. Structural modification with optimal alkyl chains not only improved the sanshool loading capacity through hydrophobic interactions but also facilitated efficient cellular internalization. Furthermore, the nanocarrier system successfully preserved the bioactivity of sanshool, allowing continuous regulation of cell cycle progression, whereas the inherent biocompatibility of the HA backbone minimized potential adverse effects. This integrated approach of molecular design and nanocarrier engineering collectively contributed to SO1's superior performance in photodamage protection through cell cycle regulation, validating the importance of carbohydrate-based material strategies in enhancing the therapeutic efficacy of natural compounds.

CONCLUSIONS

In summary, this study demonstrates that controlled hydrophobic modification of HA enables the synthesis of an amphiphilic polysaccharide derivative. This tailored HA-based polymer spontaneously self-assembles with sanshool into structurally defined NPs in an aqueous medium. The carbohydrate-based nanoencapsulation strategy significantly enhanced the photostability of the sanshool. Systematic *in vitro* and *in vivo* evaluations revealed that the resulting NPs conferred superior photoprotective effects compared with free sanshool, effectively mitigating UVB-induced oxidative stress and inflammatory responses. Notably, beyond the expected protective outcomes, this nanosystem also exhibited emergent biological activity by effectively restoring the UVB-disrupted cell cycle progression. This work not only provides a polysaccharide-engineered solution to improve the stability and delivery of natural bioactive compounds but also expands the mechanistic understanding of their multifunctional roles in skin photoprotection.

Conflict of Interests

The authors declare no conflict of interest.

Electronic Supplementary Information

Electronic supplementary information (ESI) is available free of charge in the online version of this article at http://doi.org/10.1007/s10118-026-3657-y.

Data Availability Statement

The data that support the findings of this study are available from the corresponding author upon reasonable request. The author's contact information: guzhipeng2019@scu.edu.cn.

ACKNOWLEDGMENTS

This work was financially supported by the National Natural Science Foundation of China (Nos. 524B2031 and 52422317) and the Special Research Project in Traditional Chinese Medicine (No. 2023MS099).

REFERENCES

1 Abd-Elghany, A. A.; Mohamad, E. A. Chitosan-coated niosomes loaded with ellagic acid present antiaging activity in a skin cell line. *ACS Omega* **2023**, *8*, 16620–16629.
2 Lee, S. C.; Tran, T. M. T.; Choi, J. W.; Won, K. Lignin for white natural sunscreens. *Int. J. Biol. Macromol.* **2019**, *122*, 549–554.
3 Sun, F.; Niu, H.; Wang, D.; Wu, Y.; Mu, H.; Ma, L.; Duan, J. Novel moisture-preserving derivatives of hyaluronan resistant to hyaluronidase and protective to UV light. *Carbohydr. Polym.* **2017**, *157*, 1198–1204.
4 Qureshi, S.; Chandra, S.; Chopra, D.; Dubey, D.; Jain, V.; Roy, S. K.; Ray, R. S. Nabumetone induced photogenotoxicity mechanism mediated by ROS generation under environmental UV radiation in human keratinocytes (HaCaT) cell line. *Toxicol. Appl. Pharmacol.* **2021**, *420*, 115516.
5 Bashir, M. M.; Sharma, M. R.; Werth, V. P. UVB and proinflammatory cytokines synergistically activate TNF-α

Graphical Abstract

Amphiphilic Hyaluronic Acids Enhance Sanshool's Efficacy against Skin Photodamage *via* Stability Improvement and Cell Cycle Regulation

Yi Yang, Jun-Mei Song, Tian-You Wang, Shu-Wei Wu, Yu-Hang Zhou, Zhi-Peng Gu, Ling-Hong Guo, and Xian Jiang

Sichuan University; West China Hospital

Hydrophobically modified hyaluronic acid self-assembles with sanshool into nanoparticles that scavenge ROS, inhibit apoptosis, modulate autophagy, restore cell cycle, and enable multi-target photoprotection.

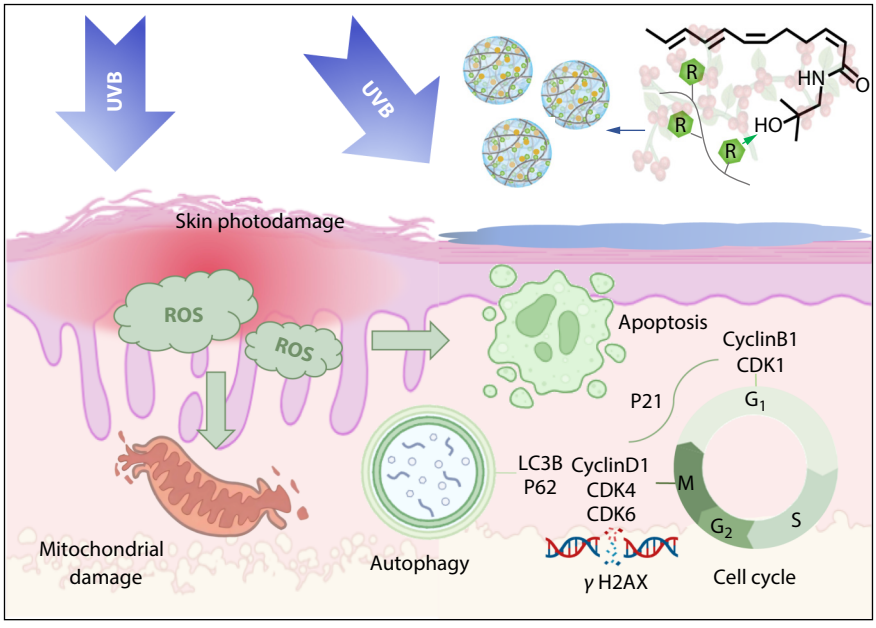

Chinese J. Polym. Sci., 2026 *https://doi.org/10.1007/s10118-026-3657-y*

production in keratinocytes through enhanced gene transcription. *J. Invest. Dermatol.* **2009**, *129*, 994–1001.

6 Cadet, J.; Douki, T. Formation of UV-induced DNA damage contributing to skin cancer development. *Photochem. Photobiol. Sci.* **2020**, *17*, 1816–1841.

7 Shin, D. W. Various biological effects of solar radiation on skin and their mechanisms: implications for phototherapy. *Anim Cells Syst* **2020**, *24*, 181–188.

8 Ashrafizadeh, M.; Mirzaei, S.; Gholami, M. H.; Hashemi, F.; Zabolian, A.; Raei, M.; Hushmandi, K.; Zarrabi, A.; Voelcker, N. H.; Aref, A. R.; Hamblin, M. R.; Varma, R. S.; Samarghandian, S.; Arostegi, I. J.; Alzola, M.; Kumar, A. P.; Thakur, V. K.; Nabavi, N.; Makvandi, P.; Tay, F. R.; Orive, G. Hyaluronic acid-based nanoplatforms for doxorubicin: a review of stimuli-responsive carriers, co-delivery and resistance suppression. *Carbohydr. Polym.* **2021**, *272*, 118491.

9 Waqas, M.; Saif, M. S.; Batool, S.; Ahmed, M. M.; Tariq, T.; Hussain, R.; Mustafa, G.; Ghorbanpour, M.; Hasan, M. Green PEGylated-Sily@ZnFe$_2$O$_4$ nanocomposites for amelioration of ROS and DNA damage in rat liver. *Sci. Rep.* **2025**, *15*, 28461.

10 Garg, C.; Sharma, H.; Garg, M. Skin photo-protection with phytochemicals against photo-oxidative stress, photo-carcinogenesis, signal transduction pathways and extracellular matrix remodeling-An overview. *Ageing Res. Rev.* **2020**, *62*, 101127.

11 Wang, C.; Wang, D.; Dai, T.; Xu, P.; Wu, P.; Zou, Y.; Yang, P.; Hu, J.; Li, Y.; Cheng, Y. Skin pigmentation-inspired polydopamine sunscreens. *Adv. Funct. Mater.* **2018**, *28*, 1802127.

12 Yang, Z.; Liu, H. J.; Zhao, J. Y.; Wang, C.; Li, H. T.; Wang, X. H.; Yang, Y.; Wu, H. X.; Gu, Z. P.; Li, Y. W. UV absorption enhanced polydopamine coating. *Mater. Horiz.* **2024**, *11*, 2438–2448.

13 Yang, Z.; Wang, X. H.; Bai, W. J.; Zou, Z. K.; Wu, H. X.; Li, Y. W. Structural disruption of melanin-like polymers with boosted UV protection. *Sci. China Chem.* **2024**, *67*, 1653–1663.

14 Yang, Z.; Zhang, J. H.; Liu, H. J.; Hu, J. F.; Wang, X. H.; Bai, W. J.; Zhang, W.; Yang, Y.; Gu, Z. P.; Li, Y. W. A Bioinspired strategy toward UV absorption enhancement of melanin-like polymers for sun protection. *CCS Chem.* **2023**, *5*, 2389–2402.

15 Wang, Z.; Yuan, J.; Xu, Y.; Shi, N.; Lin, L.; Wang, R.; Dai, R.; Xu, L.; Hao, N.; Li, Q. Olea europaea leaf exosome-like nanovesicles encapsulated in a hyaluronic acid/tannic acid hydrogel dressing with dual "defense-repair" effects for treating skin photoaging. *Mater. Today Bio* **2024**, *26*, 101103.

16 Zhang, R.; Liang, B.; Bai, W. J.; Hu, J. F.; Wang, T. Y.; Yang, Y. Y.; Bai, H. W.; Yang, L.; Li, Y. W. One-component anti-aging agents. *Mater. Horiz.* **2025**, *12*, 2977–2988.

17 Liu, H.; Hu, D.; Chen, X.; Ma, W. Surface engineering of nanoparticles for highly efficient UV-shielding composites. *Polym. Adv. Technol.* **2020**, *32*, 6–16.
18 Bedian, L.; Villalba-Rodríguez, A. M.; Hernández-Vargas, G.; Parra-Saldivar, R.; Iqbal, H. M. N. Bio-based materials with novel characteristics for tissue engineering applications-A review. *Int. J. Biol. Macromol.* **2017**, *98*, 837–846.
19 Wang, T. Y.; Zhao, J. Y.; Yang, Z.; Xiong, L. D.; Li, L.; Gu, Z. P.; Li, Y. W. Polyphenolic sunscreens for photoprotection. *Green Chem.* **2022**, *24*, 3605–3622.
20 Battistin, M.; Bonetto, A.; Nicoli, F.; Torreggiani, E.; Brunetta, A.; Cesa, E.; Manfredini, S.; Baldisserotto, A.; Vertuani, S. Synthesis and evaluation of a ZnO-Chitosan adduct for safe and sustainable enhanced Ultra-Violet (UV) sunscreens protection. *Molecules* **2024**, *29*, 5204–5225.
21 Zhao, C. H.; Wu, S. Y.; Wang, H. Medicinal plant extracts targeting UV-Induced skin damage: molecular mechanisms and therapeutic potential. *Int. J. Mol. Sci.* **2025**, *26*, 2278.
22 Pizano-Andrade, J. C.; Vargas-Guerrero, B.; Gurrola-Díaz, C. M.; Vargas-Radillo, J. J.; Ruiz-López, M. A. Natural products and their mechanisms in potential photoprotection of the skin. *J. Biosciences* **2022**, *47*, 77.
23 Li, N. N.; Ji, X. H.; Mukherjee, S.; Yang, B.; Ren, Y. Q.; Wang, C. H.; Chen, Y. S. A bioinspired skin UV filter with broadband UV protection, photostability, and resistance to oxidative damage. *ACS Appl. Mater. Interfaces* **2023**, *15*, 10383–10397.
24 Hao, D.; Wen, X.; Liu, L.; Wang, L.; Zhou, X. L.; Li, Y. M.; Zeng, X.; He, G.; Jiang, X. Sanshool improves UVB-induced skin photodamage by targeting JAK2/STAT3-dependent autophagy. *Cell Death Dis.* **2019**, *10*, 19.
25 Guo, L. H.; Wang, T. Y.; Li, Z. X.; Wu, S. W.; Xu, Y. Y.; Yang, Z.; Li, Y. W.; Gu, Z. P.; Jiang, X. Melanin-like nanoparticles boosted the photoprotective efficiency and stability of sanshool. *Chem. Mater.* **2023**, *35*, 5420–5432.
26 Cunha, L. C. M.; Monteiro, M. L. G.; Lorenzo, J. M.; Munekata, P. E. S.; Muchenje, V.; de Carvalho, F. A. L.; Conte, C. A. Natural antioxidants in processing and storage stability of sheep and goat meat products. *Food Res. Int.* **2018**, *111*, 379–390.
27 Morais, R. P.; Hochheim, S.; de Oliveira, C. C.; Riegel-Vidotti, I. C.; Marino, C. E. B. Skin interaction, permeation, and toxicity of silica nanoparticles: Challenges and recent therapeutic and cosmetic advances. *Int. J. Pharmaceut.* **2022**, *614*, 121439.
28 Fralliccardi, J.; Gabba, M.; Poolman, B. Determining small-molecule permeation through lipid membranes. *Nat. Protoc.* **2022**, *17*, 2620–2646.
29 Cao, H.; Yang, L.; Tian, R.; Wu, H. X.; Gu, Z. P.; Li, Y. W. Versatile polyphenolic platforms in regulating cell biology. *Chem. Soc. Rev.* **2022**, *51*, 4175–4198.
30 Wang, T. Y.; Guo, L. H.; Wu, S. W.; Xu, Y. Y.; Song, J. M.; Yang, Y.; Zhang, H. J.; Li, D. C.; Li, Y. W.; Jiang, X.; Gu, Z. P. Polyphenolic platform ameliorated sanshool for skin photoprotection. *Adv. Sci.* **2024**, *11*, 2310012.
31 Xie, L.; Shen, M.; Hong, Y.; Ye, H.; Huang, L.; Xie, J. Chemical modifications of polysaccharides and their anti-tumor activities. *Carbohydr. Polym.* **2020**, *229*, 115436.
32 Chen, R.; Liu, Y.; Jiang, Y.; Sun, M.; Fan, Z.; Du, J. Recent advances and future prospects in biological-membrane-targeted polymers. *Polym. Sci. Technol.* **2025**, *1*, 584–606.
33 Grabowski, M.; Gmyrek, D.; Żurawska, M.; Trusek, A. hyaluronic acid: production strategies, gel-forming properties, and advances in drug delivery systems. *Gels* **2025,** *11*, 6.
34 Montanari, E.; Zoratto, N.; Mosca, L.; Cervoni, L.; Lallana, E.; Angelini, R.; Matassa, R.; Coviello, T.; Di Meo, C.; Matricardi, P. Halting hyaluronidase activity with hyaluronan-based nanohydrogels: development of versatile injectable formulations. *Carbohydr. Polym.* **2019**, *221*, 209–220.
35 Chylińska, N.; Maciejczyk, M. Hyaluronic acid and skin: its role in aging and wound-healing processes. *Gels* **2025**, *11*, 281.
36 Zhang, X. D.; Wei, D. Y.; Xu, Y.; Zhu, Q. Hyaluronic acid in ocular drug delivery. *Carbohydr. Polym.* **2021**, *264*, 118006.
37 How, K. N.; Yap, W. H.; Lim, C. L. H.; Goh, B. H.; Lai, Z. W. Hyaluronic acid-mediated drug delivery system targeting for inflammatory skin diseases: a mini review. *Front. Pharmacol.* **2020**, *11*, 1105.
38 Kim, D. S.; Choi, J. T.; Kim, C. B.; Shin, Y. R.; Park, P. G.; Kim, H.; Lee, J. M.; Park, J. H. Microneedle array patch (MAP) consisting of crosslinked hyaluronic acid nanoparticles for processability and sustained release. *Pharm. Res.* **2020**, *37*, 50.
39 Bokatyi, A. N.; Dubashynskaya, N.; Skorik, Y. A. Chemical modification of hyaluronic acid as a strategy for the development of advanced drug delivery systems. *Carbohydr. Polym.* **2024**, *337*, 122145.
40 Hu, M.; Tang, Y.; He, X.; Liu, K.; Qin, L.; Wang, X.; Wang, Q. Enzyme-integrated hydrogels for advanced biological applications. *Polym. Sci. Technol*. **2025,** doi.org/10.1021/polymscitech.5c00076.
41 Guo, P.; Dong, L.; Xue, B.; Cao, Y.; Yang, J. From light to life: molecular mechanisms and macroscopic transformations in photoresponsive hydrogels. *Polym. Sci. Technol.* **2025**, *1*, 812–831.
42 Carvalho, A. M.; da Costa, D. S.; Reis, R. L.; Pashkuleva, I. RHAMM expression tunes the response of breast cancer cell lines to hyaluronan. *Acta Biomater.* **2022**, *146*, 187–196.
43 Amorim, S.; Reis, C. A.; Reis, R. L.; Pires, R. A. Extracellular matrix mimics using hyaluronan-based biomaterials. *Trends Biotechnol.* **2021**, *39*, 90–104.
44 Anwar, A.; Anwar, H.; Yamauchi, T.; Tseng, R.; Agarwal, R.; Horwitz, L. D.; Zhai, Z. L.; Fujita, M. Bucillamine inhibits UVB-induced MAPK activation and apoptosis in human HaCaT keratinocytes and SKH-1 hairless mouse skin. *Photochem. Photobiol.* **2020**, *96*, 870–876.
45 Ornatowski, W.; Lu, Q.; Yegambaram, M.; Garcia, A. E.; Zemskov, E. A.; Maltepe, E.; Fineman, J. R.; Wang, T.; Black, S. M. Complex interplay between autophagy and oxidative stress in the development of pulmonary disease. *Redox Biol.* **2020**, *36*, 101679.
46 Jiang, M.; Yang, S. Z.; Zhang, X. Y.; Zhang, L. Z.; Gong, J. S.; Han, T. T.; Chen, Y.; Wang, X. N.; Shi, J. S. Protective effect of ferulic acid-hyaluronic acid copolymer against UVB irradiation in a human HaCaT cell line. *Int. J. Biol. Macromol.* **2024**, *279*, 135570.
47 Sul, O. J.; Ra, S. W. Quercetin prevents LPS-induced oxidative stress and inflammation by modulating NOX2/ROS/NF-kB in lung epithelial cells. *Molecules* **2021**, *26*, 6949–6960.
48 Pu, Z. C.; Wang, W. H.; Xie, H. T.; Wang, W. S. Apolipoprotein C3 (ApoC3) facilitates NLRP3 mediated pyroptosis of macrophages through mitochondrial damage by accelerating of the interaction between SCIMP and SYK pathway in acute lung injury. *Int. Immunopharmacol.* **2024**, *128*, 111537.
49 Thielhelm, T. P.; Goncalves, S.; Welford, S.; Mellon, E. A.; Bracho, O.; Estivill, M.; Brown, C.; Morcos, J.; Ivan, M. E.; Telischi, F.; Fernandez-Valle, C.; Dinh, C. T. Primary vestibular schwannoma cells activate p21 and RAD51-associated DNA repair following radiation-induced DNA damage. *Otol. Neurotol.* **2021**, *42*, E1600–E1608.
50 Bury, M.; Le Calvé, B.; Ferbeyre, G.; Blank, V.; Lessard, F. New insights into CDK regulators: novel opportunities for cancer therapy. *Trends Cell Biol.* **2021**, *31*, 331–344.
51 Huang, M.; Zou, J.; Luo, B.; Sun, Y.; Yang, Z.; Kong, H.; Long, X.; Sun, X.; Yang, M.; Wang, X.; Liu, X.; Zhao, X. p14ARF interacts with γ-H2AX and is involved in the DNA damage response. *Biochem. Biophys. Res. Commun*. **2025,** *765*, 151847.
52 Karimian, A.; Ahmadi, Y.; Yousefi, B. Multiple functions of p21 in cell cycle, apoptosis and transcriptional regulation after DNA damage. *DNA Repair* **2016**, *42*, 63–71.